IEEE Access
Multidisciplinary | Rapid Review | Open Access Journal

Received March 10, 2021, accepted March 25, 2021, date of publication April 2, 2021, date of current version April 16, 2021.

Digital Object Identifier 10.1109/ACCESS.2021.3070658

A Dynamic-Data-Driven Method for Improving the Performance of Receiver Autonomous Integrity Monitoring

XUEEN ZHENG[1], CHENGDONG XU[2], YUDONG WANG[3], HAOMING ZOU[4], XIJUAN LV[4], SHUAI ZHAO[4], YANSONG SHI[4], AND QINGHAI SHU[4]

[1]School of Mechatronical Engineering, Beijing Institute of Technology, Beijing 100081, China
[2]School of Aerospace Engineering, Beijing Institute of Technology, Beijing 100081, China
[3]Beijing Aerospace Long March Aircraft Research Institute, Beijing 100076, China
[4]School of Materials Science and Engineering, Beijing Institute of Technology, Beijing 100081, China

Corresponding author: Qinghai Shu (qhshu121@bit.edu.cn)

This work was supported in part by the Fundamental Research Funds for the Central Universities under Grant 2017CX10003.

ABSTRACT In this article, the problem of receiver autonomous integrity monitoring (RAIM) is transformed into a modeling problem using dynamic data and an artificial neural network. A new RAIM method based on a probabilistic neural network (P-RAIM) is presented to improve integrity monitoring performance. Compared with existing RAIM methods, P-RAIM has a greater ability to meet the monitoring requirements for localizer performance with vertical guidance down to altitudes of 250 feet (LPV-250) in a single global navigation satellite system. First, by projecting the pseudorange error model from the measurement domain into the positioning domain through multiconvolution, patterns including a satellite fault pattern and a fault-free pattern are obtained based on variance inflation theory. Second, the P-RAIM model is proposed as a modified dynamic-data-driven probabilistic neural network with five layers; moreover, unique methods for training sample collection and integrity support are presented. Then, particle swarm optimization is applied to optimize a fitness function based on the false alarm probability and missed detection probability thereby improving the ability of P-RAIM to meet the LPV-250 requirements, including the false alarm probability, missed detection probability, vertical alarm limit and alarm time. Finally, utilizing real satellite data from a receiver located in Beijing to verify the effectiveness and universality of P-RAIM, evaluation experiments show that both the false alarm probability and missed detection probability can be effectively reduced to meet the LPV-250 requirements when the positioning bias is no less than 40 m. Compared with least-squares-residuals RAIM, P-RAIM can more easily detect potential faulty satellites in a single constellation.

INDEX TERMS Receiver autonomous integrity monitoring, LPV-250, global navigation satellite system, multi-layer neural network, alarm systems.

I. INTRODUCTION

When a global navigation satellite system (GNSS) is used for positioning, its integrity must be evaluated to ensure the reliability of the positioning results [1], [2]. Receiver autonomous integrity monitoring (RAIM) is a method of checking satellite integrity that is independently performed by receivers to provide real-time protection for users [3]. When a satellite navigation system fails or cannot meet the required positioning accuracy, the RAIM function promptly alerts users so as to avoid accidents [4].

The associate editor coordinating the review of this manuscript and approving it for publication was Zhaojun (Steven) Li.

Pseudorange bias caused by satellite faults can result in erroneous positioning [5]. RAIM depends on the measured noise and the false alarm probability (FAP) to detect satellite faults [6]. Two styles of RAIM have attracted attention: the least-squares-residuals approach and the Bayes approach. First, RAIM based on classical least-squares theory was used to detect single faults in the Global Positioning System (GPS) [7], [8]. At the same time, Sturza [9] projected the observation matrix into the parity space and solved the fault detection problem using a parity method. This method was demonstrated to have the same performance as least-squares-residuals RAIM (LSR-RAIM). Since then, many studies have been devoted to improving the monitoring performance of

RAIM. For example, Joerger *et al.* [10] proposed a non-least-squares-residuals method to reduce the missed detection probability (MDP), and Brown [11] proposed a multiple-hypothesis solution separation algorithm that could deal with multiple-fault detection in the case of multiple constellations. Based on this method, in 2012–2016, a research group [12], [13] formed by the Federal Aviation Administration and the European Space Agency developed the Advanced RAIM (ARAIM) algorithm [14], which has the potential to meet the navigational requirements for localizer performance with vertical guidance down to altitudes of 250 feet (LPV-250) [15] when both GPS and Galileo are applied in an integrated manner [16].

Second, following least-squares theory, RAIM algorithms based on Bayesian detection theory has also seen rapid development. Researchers have attempted to improve the efficiency of detection in various ways. For example, Pesonen [17] proposed a RAIM method relying on Bayesian theory to detect single-satellite faults and developed a framework in which the problem of evaluating satellite navigation integrity is transformed into the problem of estimating a posterior probability distribution for the positioning parameters. Zhang and Gui [18] presented a RAIM method for multisatellite fault detection that is also based on a Bayesian hypothesis testing framework. Satellite faults can be determined by calculating the probabilities of hazardously misleading information. In 2020, Sun [19] attempted to utilize artificial neural networks to detect faulty satellites and proposed a RAIM approach based on a deep neural network.

Many researchers [20] have devoted efforts to reducing the missed detection probability and alarm limit of RAIM in order to meet the stringent LPV-250 navigation requirements. Among existing methods, multiconstellation ARAIM with integrity support messages has the potential to be used for LPV-250; however, the availability of single-constellation ARAIM [21] is low, so there is still a need to develop single-constellation RAIM methods that can meet the monitoring requirements for LPV-250 [22], [23]. In reference [24], although we attempted to achieve the critical value of the characteristic slope to reduce the fault detection risk of the LSR algorithm, it was still difficult to use LSR-RAIM for LPV-250 in a single constellation. In this paper, following the ARAIM algorithm, integrity support messages were used to model the pseudorange error distribution [25], and we used big data techniques to sample a large amount of data from the error distribution model to train an artificial neural network (e.g., a probabilistic neural network) to monitor GPS integrity.

Probabilistic neural networks (PNNs) have been widely used for data classification and pattern recognition [26]. Essentially, the detection of satellite faults is a pattern recognition problem; thus, it is feasible to introduce PNN techniques into satellite fault detection. However, few related studies have been published, mainly because fault samples for satellites are extremely rare, with no more than three failures annually. Moreover, satellite failures are complex, and identical failures rarely occur repeatedly, making it almost impossible to train a PNN on fault samples. Thus, developing a solution for selecting fault samples and training a corresponding PNN model is of key importance for integrity monitoring.

In this paper, a new RAIM method based on a probabilistic neural networks (P-RAIM) is presented for integrity monitoring. First, we propose a modeling method based on a fault model and a fault-free model. In this method, the pseudorange noise in the measurement domain is assumed to follow a normal distribution with zero mean and unknown variance [27], and we project the noise model into the position domain via a multiple convolution formula. In accordance with variance inflation theory, a fault-free model is derived from the position precision, and a fault model is derived from the inflation factor. Thus, integrity monitoring is formulated as a problem of determining whether the statistical model of the position error includes the inflation factor.

Then, we propose the structure of P-RAIM. It has five layers: an input layer, a pattern layer, an averaging layer, a comparison layer, and an output layer. Unlike other methods, P-RAIM is based on variance expansion and focuses on the differences arising from a group of position values.

Third, we propose a training method for P-RAIM. The training method consists of two stages: collecting training samples and optimizing P-RAIM. To ensure that the detection performance of P-RAIM meets the LPV-250 navigation requirements [28], particle swarm optimization (PSO) is utilized to search for the optimal value of the fitness function, which is based on the false alarm probability and the missed detection probability, and an optimal smoothing parameter λ is selected to improve the integrity of P-RAIM.

Finally, the P-RAIM method is verified to be superior to LSR-RAIM [24] on the basis of GPS data received over 24 hours.

II. METHODOLOGY

A. CLASSIFICATION MODEL BASED ON VARIANCE EXPANSION

Let n denote the number of visible satellites, and let the linearized single-point positioning equation be:

$$\mathbf{y} = \mathbf{G}\mathbf{x} + \mathbf{e} \tag{1}$$

where $\mathbf{y}$ is an $n \times 1$ vector of observations containing the differences between the expected ranging values and the raw pseudorange observations to each of the n satellites. $\mathbf{x}$ is an $m \times 1$ vector that expresses the three components of the correct position deviation from the nominal position and the clock bias between the receiver and constellation; when a single constellation is used for positioning, $m = 4$. $\mathbf{G}$ is an $n \times m$ observation matrix, and $\mathbf{e} = (e_1, \cdots\cdots, e_n)^T$ is the $n \times 1$ vector of measurement residuals. In general, the statistical model of $\mathbf{e}$ is considered to be $\mathbf{e} \sim N(0, \sum)$, where $\sum$ is a covariance matrix with diagonal elements σ_i^2. $\mathbf{b} = (b_x, b_y, b_z, b_t)^T$ is the 4×1 vector containing the position

errors and clock error, which are given by:

$$\mathbf{y} = \mathbf{G}\tilde{\mathbf{x}} \tag{2}$$

$$\tilde{\mathbf{x}} = (\mathbf{G}^{\mathbf{T}}\mathbf{G})^{-\mathbf{1}}\mathbf{G}^{\mathbf{T}}\mathbf{y} \tag{3}$$

$$\mathbf{b} = \mathbf{x} - \tilde{\mathbf{x}} = -(\mathbf{G}^{\mathbf{T}}\mathbf{G})^{-\mathbf{1}}\mathbf{G}^{\mathbf{T}}\mathbf{e} \tag{4}$$

where $\tilde{\mathbf{x}}$ represents the estimated value of $\mathbf{x}$, which includes the positioning error. We assume that $\mathbf{A} = -(\mathbf{G}^{\mathbf{T}}\mathbf{G})^{-\mathbf{1}}\mathbf{G}^{\mathbf{T}}$ and rewrite (4) as:

$$\mathbf{b} = \mathbf{A}\mathbf{e} \tag{5}$$

According to (5), b_{x}, b_{y}, and b_{z} can be expressed as:

$$\mathbf{b}(j) = \sum_{i=1}^{n} a_{ji}e_i, \quad (j \in \{1, 2, 3\}, i \in \{1, \cdots, n\}) \tag{6}$$

where $e_i \sim N(0, \sigma_i^2)$ and the a_{ji} are constants. The statistical model of b in the position domain can be obtained from that of e in the measurement domain. The multiple convolution formula given in (7) is used to obtain b_{x}; expressions for b_{y} and b_{z} are obtained in a similar manner.

$$\begin{aligned} f_{bx}(b_x 4) = & \underbrace{\int_{-\infty}^{+\infty} \cdots \int_{-\infty}^{+\infty}}_{n-1} f_{e_1}(a_{11}e_1) \cdots f_{e_{i-1}}(a_{1,i-1}e_{i-1}) \\ & \times f_{e_{i+1}}(a_{1,i+1}e_{i+1}) \cdots f_{e_n}(a_{1n}e_n) \\ & \times f_{e_i}(b_x - \sum\nolimits_{j=1}^{n-i} a_{1j}e_j) de_1 de_{i-1} de_{i+1} de_n \end{aligned} \tag{7}$$

where f_{e_i} and f_{bx} represent the marginal probability density functions of e_i and b_x, respectively, and $n_{-i} = (1, \cdots, i-1, i+1, \cdots, n)$. When each e_i is assumed to be independent of the others, $\mathbf{b} \sim N(0, \sum_{position})$ and $\sum_{position} = (\sigma_x^2, \sigma_y^2, \sigma_z^2)^T$, where the diagonal elements σ_x^2, σ_y^2 and σ_z^2 are calculated as:

$$\sum\nolimits_{position}(j) = \sum_{i=1}^{n} a_{ji}^2\sigma_i^2, \quad (j \in \{1, 2, 3\}, i \in \{1, \cdots, n\}) \tag{8}$$

If the fault value f from a satellite is regarded as a random variable, it can be considered that the variance of $\mathbf{b}_f$ containing a fault value will be enlarged, but the mean will not be biased [29]. In this case, $\mathbf{b}_f \sim N(0, k^2 \sum_{position})$, where k is called the inflation factor.

When a set of positioning data is collected as a sample, s_x^2, s_y^2, and s_z^2 are the sample variances of the position values on the three axes. The model for fault detection can be expressed as:

$$s_j = \begin{cases} \sigma_j & b_j \sim N(0, \sigma_j^2) \\ k\sigma_j & b_j \sim N(0, k^2\sigma_j^2), \end{cases} \quad (j \in \{x, y, z\}) \tag{9}$$

Thus, the problem of satellite fault detection has been transformed into one of identifying a statistical model of random variables. In accordance with the principle of Bayesian hypothesis testing [30], when $P(s_j = \sigma_j)/P(s_j = k\sigma_j) > 1$, we consider $s_j = \sigma_j$ to be more credible, indicating that b_j is normal. Otherwise, if $P(s_j = k\sigma_j) > P(s_j = \sigma_j)$, b_{x} is identified as containing a fault.

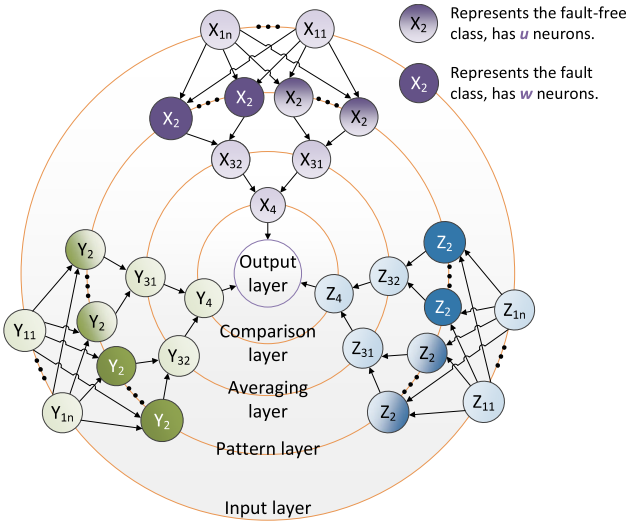

FIGURE 1. The network structure of P-RAIM.

B. STRUCTURE OF P-RAIM

The five layers of P-RAIM are described as follows (see Fig. 1).

1. The input layer is used to store the position data collected by the receiver; typically, the number of data is greater than 30. The input layer is divided into three parts corresponding to the x-axis, y-axis, and z-axis. When a satellite fails, the pseudorange fault values projected along the three axes are different from each other, depending on the geometry of the satellites used for positioning [31]. It is difficult to determine on which axis the projection value will be sufficient to be detected; therefore, the standard deviations of the position errors in all 3 dimensions are detected. The number of neurons is equal to the number of position data.

2. The pattern layer is used to calculate the standard deviation of X_1, for which the function is expressed as follows:

$$X_2 = \left(\frac{1}{n-1}\sum_{i=1}^{n}(x_i - \frac{1}{n}\sum_{j=1}^{n}x_j)^2\right)^{1/2} \tag{10}$$

where X_2 represents the value of a neuron corresponding to the x-axis. In the pattern layer, the neurons are divided into two patterns, representing the fault class and the fault-free class. The number of neurons in the pattern layer is equal to $s + w$.

3. The averaging layer calculates the value of the activation function at which the input X_2 is similar to the detected sample. In the P-RAIM model, a Gaussian function is selected as the activation function:

$$\phi(X) = \exp\left(-\frac{(X - LX)^2}{2\lambda^2}\right) \tag{11}$$

$$X_{31} = \sum_{i=1}^{s} \mathrm{e}^{\frac{|X_2 - LX_i|}{\lambda^2}} \tag{12}$$

$$X_{32} = \sum_{i=1}^{w} \mathrm{e}^{\frac{|X_2 - LXF_i|}{\lambda^2}} \tag{13}$$

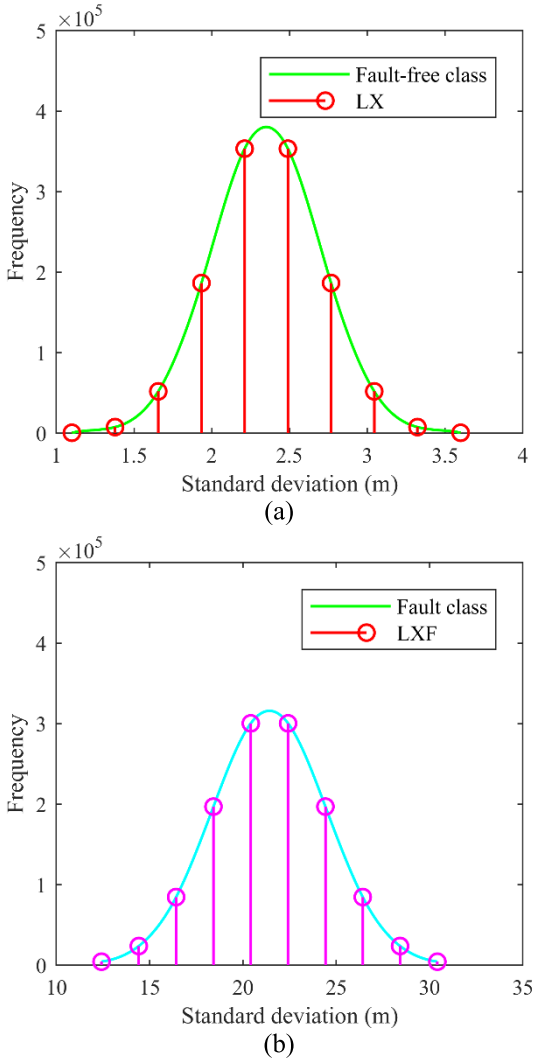

FIGURE 2. Collection of training samples from the fault-free class (LX) and the fault class (LXF).

X_{31} represents the output for the fault-free pattern, X_{32} represents the output for the fault pattern, X_2 represents the information of the input sample, *LX* represents a fault-free training sample, and *LXF* represents a faulty training sample. The number of neurons in the averaging layer is equal to the number of classes.

4. The comparison layer performs comparison calculations using the outputs of the averaging layer. f_{x1} represents the average probability of a sample belonging to the fault class, and f_{x2} represents the average probability of a sample belonging to the fault-free class.

$$f_{x1} = X_{31}/u \tag{14}$$

$$f_{x2} = X_{32}/w \tag{15}$$

$$X_4 = \begin{cases} 0 & \text{if } f_{x1} > f_{x2} \\ 1 & \text{if } f_{x1} \le f_{x2} \end{cases} \tag{16}$$

If the probability that the sample standard deviation belongs to the fault class is greater than the probability that it belongs to the fault-free class, X_4 outputs a value of 1. Otherwise, X_4 will output 0. This layer has three neurons. The modeling approach for Y_2, Y_{31}, Y_{32}, and Y_4 on the y-axis and Z_2, Z_{31}, Z_{32}, and Z_4 on the z-axis is the same as that for X_2, X_{31}, X_{32}, and X_4 on the x-axis.

5. The output layer performs Boolean OR operations on the x-axis, y-axis and z-axis output values from the comparison layer and produces the final detection result. An output R value of 1 indicates that the satellite used for positioning has a fault, and 0 indicates that the satellite is fault free. There is one neuron in the output layer.

$$R = X_4 \wedge Y_4 \wedge Z_4 \tag{17}$$

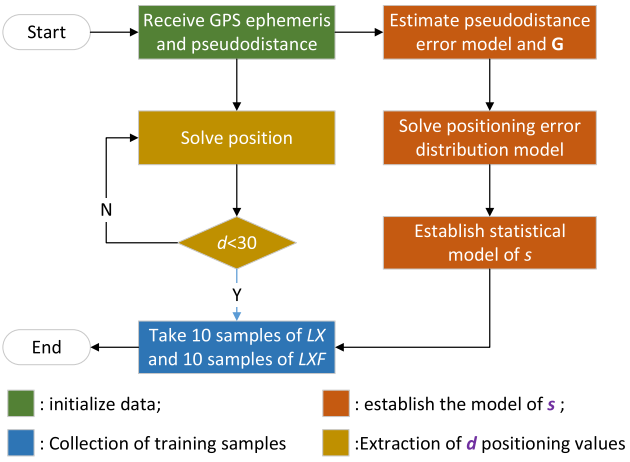

FIGURE 3. Process of collecting training samples.

C. TRAINING OF P-RAIM

1) COLLECTION OF TRAINING SAMPLES BASED ON DYNAMIC-DATA-DRIVEN ANALYSIS

The training samples should include both fault-free samples and fault samples. Fault-free samples are used to represent the statistical model of the standard deviation of a group of normal positioning values, whereas fault samples are used for fault positioning values. Such samples can be obtained by sampling data from a model of the position error distribution (PED). Affected by the number of satellites and the elevation angle, the PED is dynamic; as a result, the training samples will also be dynamic.

Suppose that d samples are extracted from the PED to form a sample group $\mathbf{M}$. When d is less than 30, the standard deviation s of $\mathbf{M}$ can be described as:

$$s \sim W(a, b, c) \tag{18}$$

where $W(a, b, c)$ is the three-parameter Weibull distribution and a, b, and c are given in reference [32]. When d is greater than 30, the statistical model of s can be described as:

$$s \sim N(c_m\sigma, \sigma^2/(2d)) \tag{19}$$

where σ is the standard deviation of the PED and c_m is a parameter to correct the difference between the expectation of the sample standard deviation and the actual value, which can be obtained by calculating the average of the standard

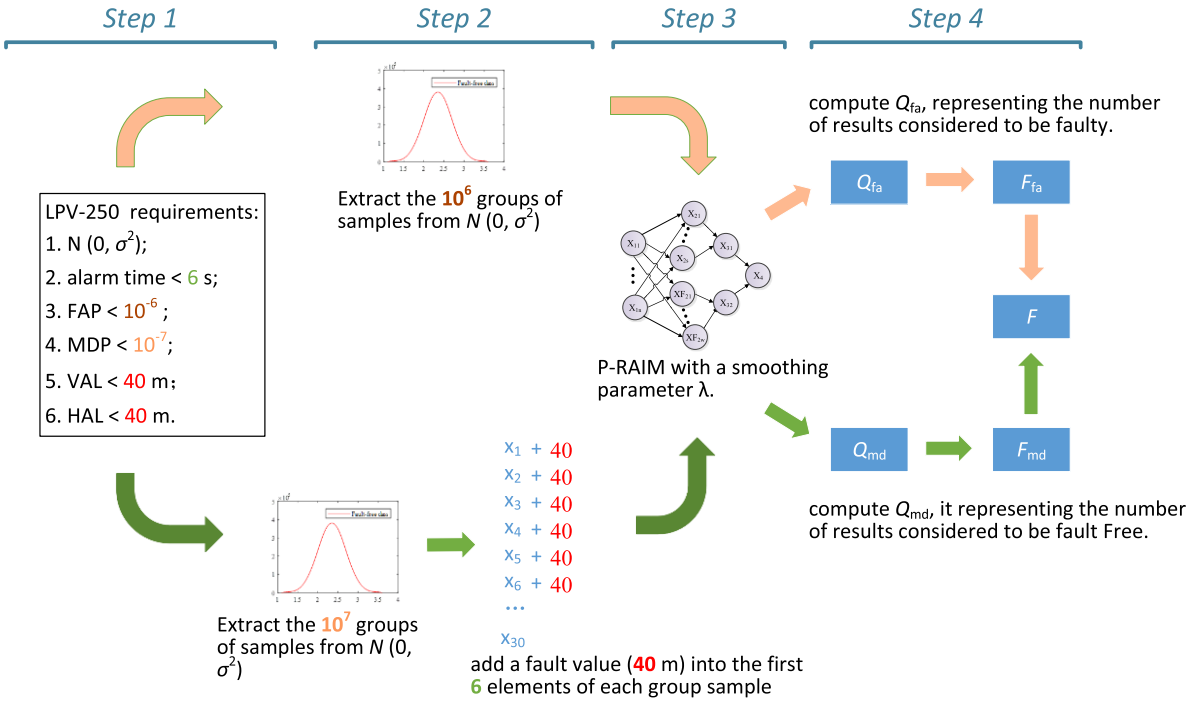

FIGURE 4. Process of computing F.

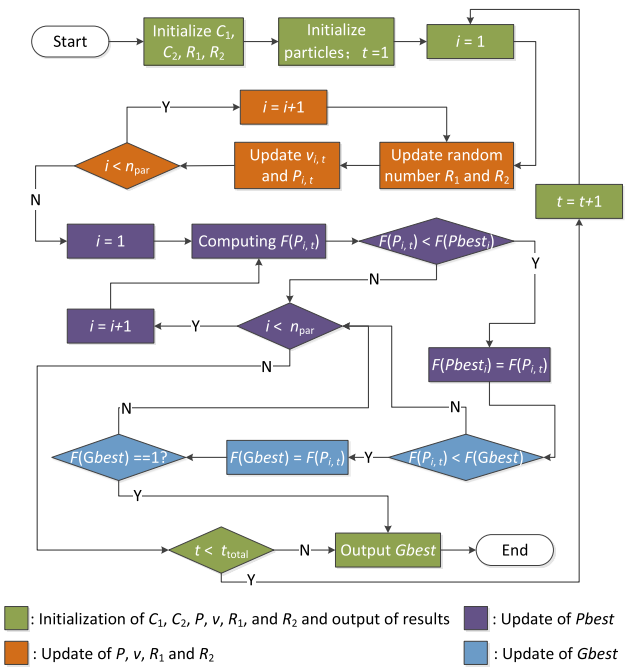

FIGURE 5. Process of using PSO to solve for λ.

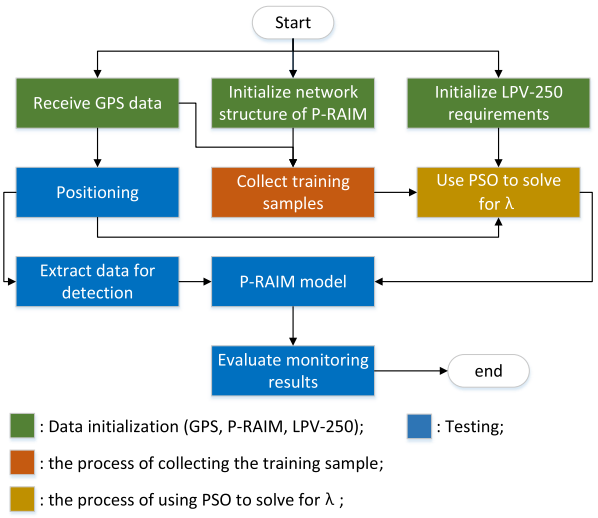

FIGURE 6. Experimental process.

deviation. For example, when $\sigma^2 = 6.5$, the distribution of s is shown in Fig. 2(a).

A set of values is selected as training samples from the fitted distribution. In the 3-sigma range of the distribution, 10 training sample values $\{LX_1, \cdots, LX_{10}\}$ for the fault-free class are selected at equal intervals. The equation is shown as follows:

$$LX_i = (C_m - \frac{3}{\sqrt{2d}} + \frac{2(i-1)}{3\sqrt{2d}})\sigma \tag{20}$$

Similarly, if $k = 9$, 10 training sample values $\{LXF_1, \cdots, LXF_{10}\}$ for the fault class are selected from the 3-sigma range of the corresponding distribution, as shown in Fig. 2(b). The equation is shown as follows:

$$LXF_i = (C_m - \frac{3}{\sqrt{2d}} + \frac{6(i-1)}{(w-1)\sqrt{2d}})k\sigma \tag{21}$$

TABLE 1. Performance indexes of P-RAIM.

Performance index	Value
false alarm probability (FAP)	10^{-6}
missed detection probability (MDP)	10^{-7}
vertical alarm limit (VAL)	40 m
horizontal protection limit	40 m
alarm time (AT)	6 s

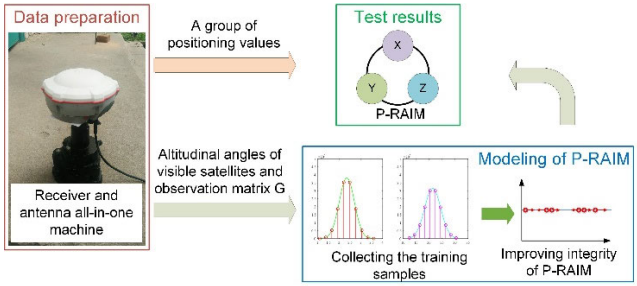

FIGURE 7. P-RAIM testing process.

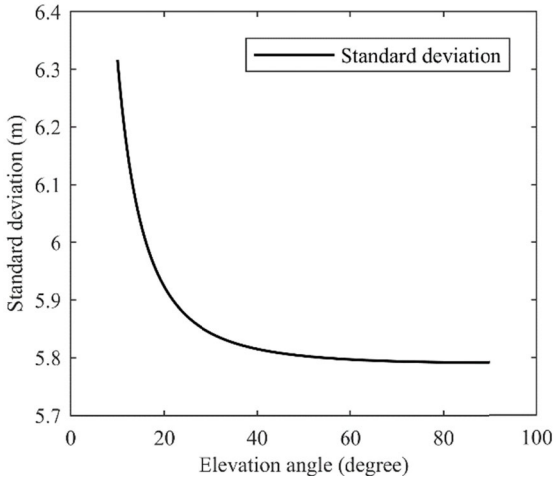

FIGURE 8. Relationship between the measurement precision σ^2 and the elevation angle.

TABLE 2. Standard deviation parameters [36].

Standard deviation	Value
user ranging accuracy (URA)	2.4 m (from the broadcast ephemeris)
residual tropospheric error*	$0.12\times1.001/(0.002001+\sin^2\alpha)^{1/2}$
multipath error*	$0.13+0.53e^{-\alpha/10}$ m
receiver noise*	$0.04-0.02\times(\alpha-5)/85$ m

*: α is the satellite elevation angle in degrees

Fig. 3 shows the process of collecting the training samples, which consists of 4 steps.

2) ENHANCING THE INTEGRITY OF P-RAIM THROUGH PSO

The smoothing parameter λ affects the performance of a PNN [33]; thus, the detection accuracy of P-RAIM can be improved by selecting an appropriate λ [34]. In this section, the detection efficiency of P-RAIM is optimized to meet

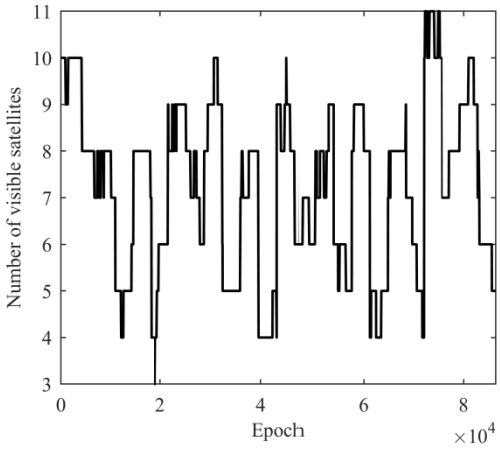

FIGURE 9. Number of visible satellites at the data collection point.

TABLE 3. List of test items.

Number of visible satellites	G1	G17	G30
Fault value	50 m	40 m	30 m
Epoch	100	500	1000
Duration	6 s	6 s	6 s

the requirements for LPV-250, including the false alarm probability, missed detection probability, vertical alarm limit (VAL) and alarm time (AT). The fitness function $F(P_i)$ is given by:

$$F(P_i) = 1\Big/(1 + F_{\mathrm{fa}}(P_i) + F_{\mathrm{md}}(P_i)) \tag{22}$$

where $F_{\mathrm{fa}}(P_i)$ and $F_{\mathrm{md}}(P_i)$ are piecewise functions:

$$F_{\mathrm{fa}}(P_i) = \begin{cases} Q_{\mathrm{fa}}(P_i) & if\ Q_{\mathrm{fa}}(P_i) > 4 \\ 0 & if\ Q_{\mathrm{fa}}(P_i) \le 4 \end{cases} \tag{23}$$

$$F_{\mathrm{md}}(P_i) = \begin{cases} Q_{\mathrm{md}}(P_i) & if\ Q_{\mathrm{md}}(P_i) > 1 \\ 0 & if\ Q_{\mathrm{md}}(P_i) \le 1 \end{cases} \tag{24}$$

where P_i represents the i-th λ value, F_{fa} is the function for the false alarm probability, F_{md} is the function for the missed detection probability, and Q is a counter. Q_{fa} is used to count the number of results that are identified as belonging to the fault class by P-RAIM, and Q_{md} is used to count the number of fault-free results. The constraint conditions, including the false alarm probability, missed detection probability, vertical alarm limit and alarm time, are used to calculate the fitness function F to improve the detection performance of P-RAIM. The process is described below.

Step 1: Initialize the performance requirements of P-RAIM and provide the statistical model of e.

Step 2: Extract samples.

Step 3: Utilize P-RAIM with a smoothing parameter λ to detect faulty samples and fault-free samples, respectively.

Step 4: Compute Q_{fa}, Q_{md}, F_{fa}, F_{md} and F.

PSO is used to select the optimal λ. PSO is a swarm intelligence method that uses a particle swarm to search for potential solutions to an optimization problem in a given

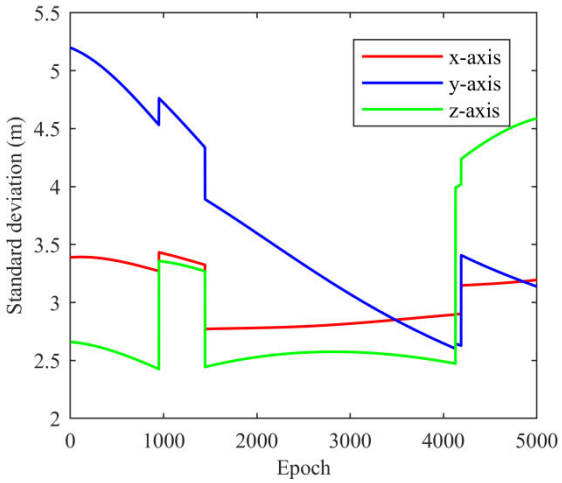

FIGURE 10. Standard deviations of position errors along the three axes.

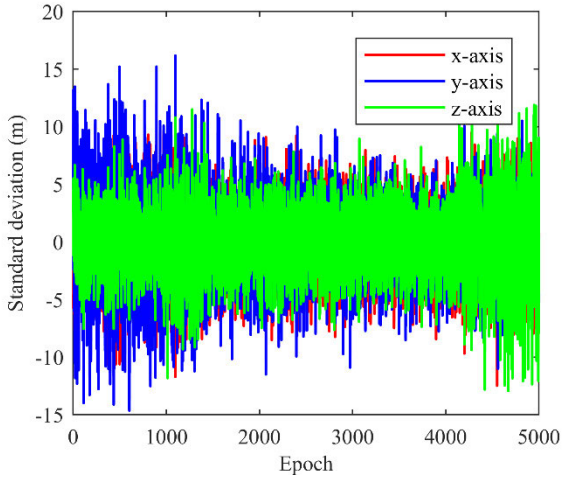

FIGURE 11. Correct positioning in all three coordinates.

search space [35]. The mathematical model is expressed as:

$$v_{i+1} = \omega \times v_i + C_1 \times R_1 \times (Pbest_i - P_i) + C_2 \times R_2 \times (Gbest - P_i) \quad (25)$$

$$P_{i+1} = P_i + v_{i+1} \quad (26)$$

where P is the objective λ value (also called the particle position in PSO), v is the update parameter (also called the particle velocity in PSO), *Pbest* is the local optimum value, *Gbest* is the global optimum value, ω is an inertia factor, C_1 and C_2 are constants, and R_1 and R_2 are random numbers in the range 0-1. Equation (25), which is used to update the velocity, is the core of the PSO algorithm and determines the search performance. When the particles adjust their positions, the positions and velocities should be limited to a certain space to maintain the search capability of the particles. The process of optimizing λ is shown in Fig. 5.

At the beginning of the algorithm, the positions, velocities and other parameters are initialized. The velocity of a particle determines the position of that particle in the next iteration, and the particle information is updated via *Pbest* and *Gbest*. The particles iteratively search for better solutions in the solution space near the current optimal particle. If $F(Gbest) < 1$, then the positions and velocities of the particles will be updated. When the fitness value is 1 ($F(Gbest) = 1$), this indicates that the false alarm probability is less than $10^{-6,}$ the missed detection probability is less than 10^{-7} and the vertical alarm limit is less than 40 m; at this time, λ takes its optimal value. The performance indexes of P-RAIM are summarized in Table 1.

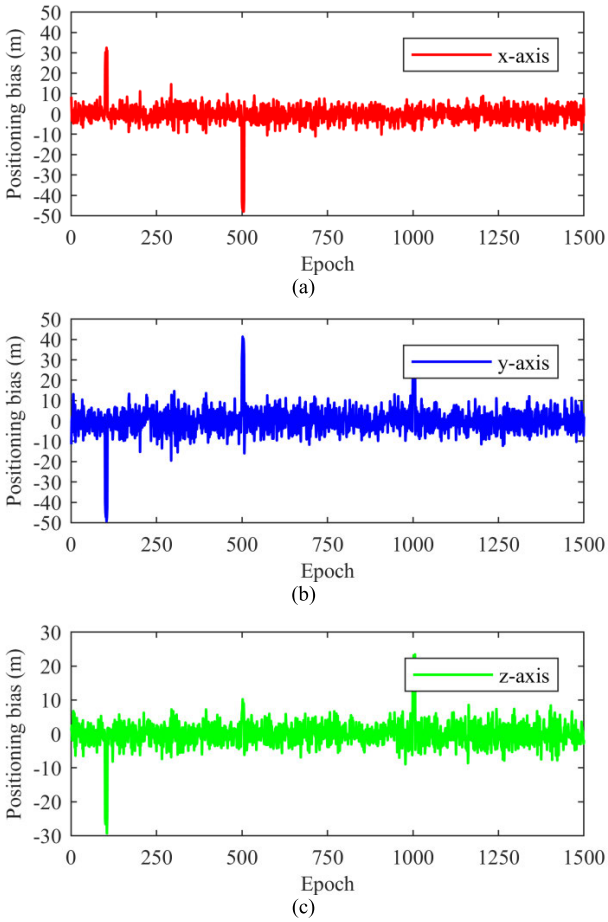

FIGURE 12. Positioning on three axes: (a) x-axis faults; (b) y-axis faults; (c) z-axis faults.

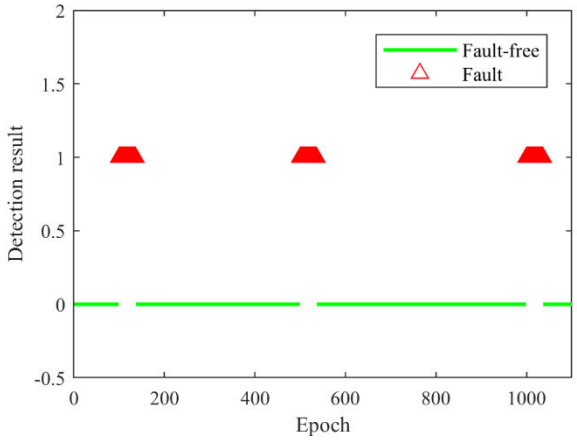

FIGURE 13. P-RAIM detection results.

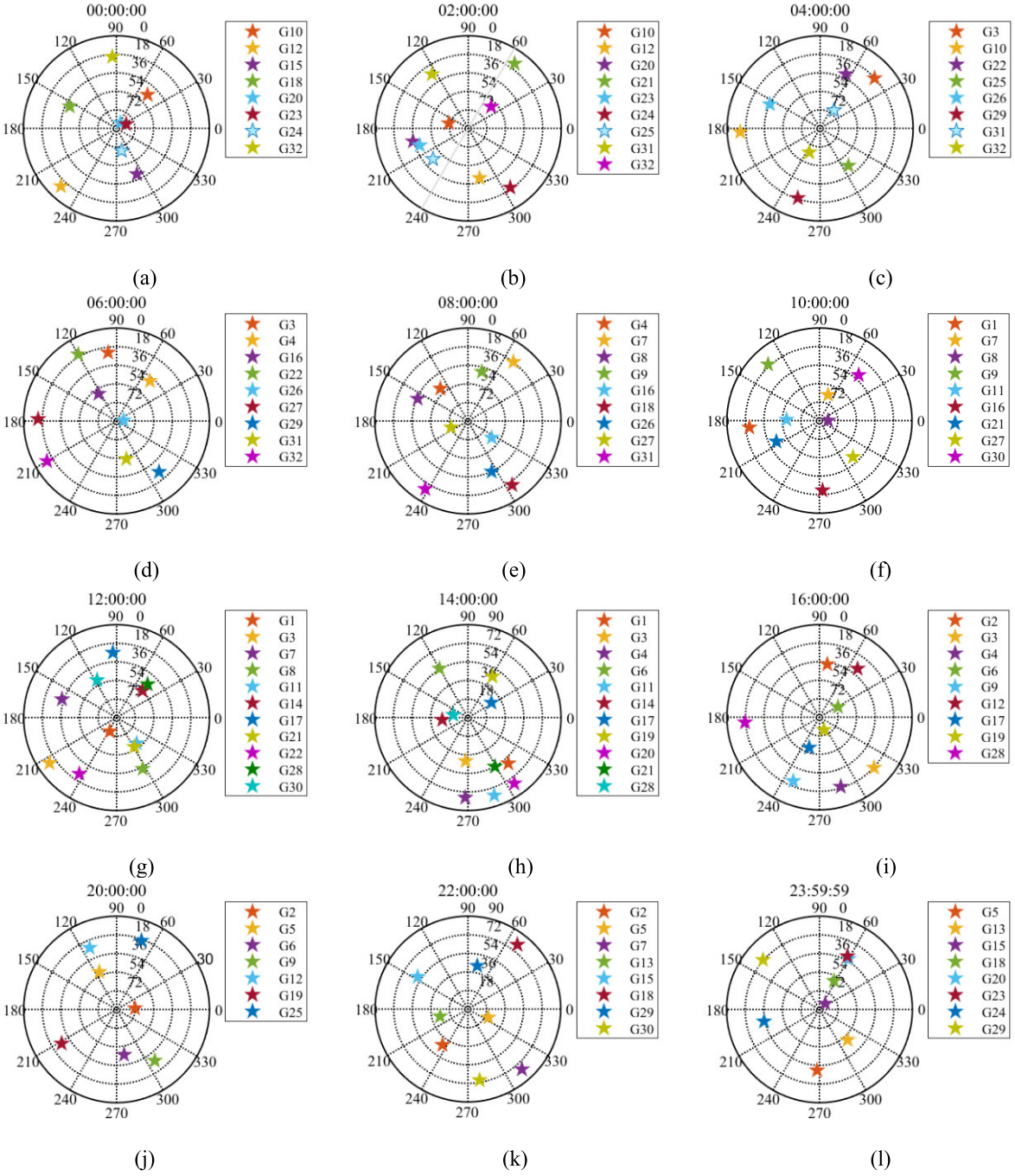

FIGURE 14. Results of 24-hour monitoring. ★ represents the detection of a fault, and ☆ represents that no fault was detected.

As described above, the final P-RAIM model is obtained by collecting training samples and optimizing λ. The experimental process, including the use of PSO to solve for λ and training on sample data, is shown in Fig. 6.

III. EXPERIMENTAL RESULTS

Real satellite data were collected using a receiver to test P-RAIM to verify its effectiveness and universality. The testing process is shown in Fig. 7.

A. DATA PREPARATION

Ephemeris data were collected from 00:00:01 to 23:59:59 on December 3, 2015, and January 27, 2021, using a T300 GNSS receiver, a high-precision multiconstellation triband receiver. The pseudorange data consisted of the true distances and random errors. The selected location was in Beijing (N: 39.95979167°, E: 116.31525278°, altitude: 58 m), and the sampling interval was 1 s; thus, 86,400 epochs were sampled throughout the day.

The measurement error is represented by $e_i \sim N(0, \sigma_i^2)$, where σ_i includes the clock/ephemeris error, residual ionospheric error, residual tropospheric error, receiver noise, and multipath error. These errors are all related to the elevation angles of the visible satellites. Table 2 shows the relationship between the standard deviation of the measurement errors and the elevation angle. As summarized in Table 2, σ_i was obtained from Fig. 8 to model $e_i \sim N(0, \sigma_i^2)$.

B. MODELING OF P-RAIM

The available satellites with elevation angles greater than 10° were selected for analysis. Fig. 9 shows the number of visible satellites over time.

Fig. 10 shows the standard deviations of the position errors on the three axes over 5000 epochs, which were computed using (8). We collected training samples for P-RAIM and used the PSO algorithm to select the optimal smoothing parameter λ. To quickly search for the optimal value, the search space was selected to be (0, 1].

C. TEST RESULTS CONCERNING THE EFFECTIVENESS OF P-RAIM

The position error model was derived from Fig. 10, and pseudorange data were simulated by adding random noise to the true range data. Faulty data were then created by artificially adding a fault value to the pseudorange data. The test items are listed in Table 3; each fault lasted for 6 s.

Fig. 11 shows correct position data with fault-free satellites, whereas Fig. 12 shows inaccurate position data with faulty satellites. Comparing these figures, we see that the positions at epochs 100, 500, and 1000 show abnormal biases after the addition of the fault value to the pseudorange data; however, the biases on the three axes are not the same. When G17 fails, no abnormal bias occurs in the z-axis positioning value, potentially resulting in an unnecessary missed detection. A similar situation occurs in epoch 1000, where the fault in G30 does not affect the positioning on the x-axis. Thus, monitoring on all three axes is necessary to ensure the detection accuracy. The P-RAIM detection results are shown in Fig. 13, where 1 denotes the occurrence of a fault in the satellites used for positioning and 0 denotes normal positioning.

D. TEST RESULTS CONCERNING THE UNIVERSALITY OF P-RAIM

To demonstrate the universality of P-RAIM, we utilized the real 24-hour ephemeris data from January 27, 2021, to monitor the integrity every 2 hours, and the results are shown in Fig. 14. A five-pointed star represents a satellite that was visible at that time, and a 40-meter fault value was added to every visible satellite. If the monitoring results indicate a fault in a satellite used for positioning, the corresponding five-pointed star shape is filled with solid color; otherwise, if the monitoring results show that a satellite used for positioning was normal, the corresponding five-pointed star is hollow. For the 106 test instances, all five-pointed stars are filled with solid color, representing that all satellites with added faults were detected correctly.

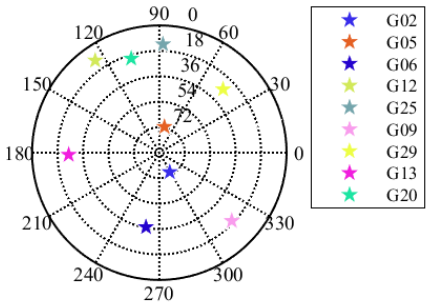

FIGURE 15. Visible satellites.

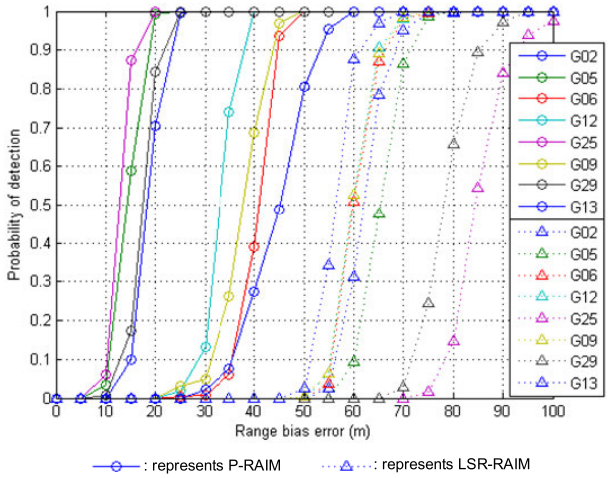

FIGURE 16. Efficiency comparison between P-RAIM and LSR-RAIM.

IV. DISCUSSION AND ANALYSIS

In this section, P-RAIM is compared with LSR-RAIM to analyze the efficiency of detection.

All visible satellites shown in Fig. 15 were tested over 600 epochs. Biases were added to every satellite, with the range biases increasing from 0 m to 100 m in steps of 5 m. The test results were sampled every 20 s. The correct detection probabilities for each satellite with P-RAIM and LSR-RAIM are shown in Fig. 16. When the range bias is less than 40 meters, the correct detection probabilities for all visible satellites are higher with P-RAIM than with LSR-RAIM. As the range bias increases, the detection probability for visible satellites with faults also gradually increases; when the range bias is greater than 60 meters, P-RAIM can identify the fault patterns of all visible satellites. Under these conditions, the detection probability with P-RAIM exceeds that with LSR-RAIM. G25 is the most potentially faulty satellite, and the range bias in G25 is hardest to detect with LSR-RAIM, whereas it is easier to detect G25 as a faulty satellite with P-RAIM. Therefore, the integrity monitoring performance of the P-RAIM exceeds that of LSR-RAIM in this test.

V. CONCLUSION

In this paper, we propose the P-RAIM method for monitoring the integrity of a GNSS based on a five-layer PNN. Based

on the theory of variance inflation, P-RAIM is used to detect the variance of the position error rather than a positioning bias. This method includes a collection method for extracting training samples from a statistical model of the standard deviation and an optimization method based on a fitness function F. To verify the applicability and universality of P-RAIM, 106 test instances over 24 hours were considered, and the results show that P-RAIM can be effectively used to monitor the integrity of a GNSS. When the pseudorange bias was no less than 40 m, P-RAIM was always effective in all tests. P-RAIM was also compared with LSR-RAIM, and the results showed that even the satellite that is the most difficult to detect as faulty with LSR-RAIM can be easily detected with P-RAIM. In particular, the detectable bias due to potential faults in P-RAIM is less than that in LSR-RAIM.

APPENDIX
DERIVATION OF THE POSITION ERROR DISTRIBUTION

As seen in (5), the position error vector is expressed as:

$$\begin{pmatrix} b_{\mathrm{x}} \\ b_{\mathrm{y}} \\ b_{\mathrm{z}} \\ b_{\mathrm{t}} \end{pmatrix} = \begin{pmatrix} a_{11} & a_{12} & \cdots & a_{1n} \\ a_{21} & a_{22} & \cdots & a_{2n} \\ a_{31} & a_{32} & \cdots & a_{3n} \\ a_{41} & a_{42} & \cdots & a_{4n} \end{pmatrix} \begin{pmatrix} e_1 \\ e_2 \\ \vdots \\ e_n \end{pmatrix} \tag{27}$$

$$b_{\mathrm{x}} = a_{11}e_1 + a_{12}e_2 + \cdots + a_{1n}e_n \tag{28}$$

We suppose that $f_{bx}(b_x)$ is the probability density function of b_{x}:

$$f_{bx}(b_x) = \int_{-\infty}^{+\infty} f(a_{11}e_1, \cdots, a_{1,n-1}e_{n-1}, b_x - \sum_{j=1}^{n-n} a_{1j}e_j) de_1 de_{n-1} \tag{29}$$

When $e_1, \ldots, e_n$ are independent, (29) can be written as:

$$f_{bx}(b_x) = \underbrace{\int_{-\infty}^{+\infty} \cdots \int_{-\infty}^{+\infty}}_{n-1} f_{e_1}(a_{11}e_1) \cdots f_{e_{n-1}}(a_{1,i-1}e_{i-1}) \times f_{e_n}(b_x - \sum_{j=1}^{n-n} a_{1j}e_j) de_1 de_{n-1} \tag{30}$$

When $e_i \sim N(0, \sigma_i^2)$, according to (30), we can derive $b_{\mathrm{x}} \sim N(0, \sigma_{\mathrm{x}}^2)$:

$$\sigma_{\mathrm{x}}^2 = a_{11}^2\sigma_1^2 + a_{12}^2\sigma_2^2 + \cdots + a_{1n}^2\sigma_n^2 \tag{31}$$

In a similar way, we can derive $b_{\mathrm{y}} \sim N(0, \sigma_{\mathrm{y}}^2)$ and $b_{\mathrm{z}} \sim N(0, \sigma_{\mathrm{z}}^2)$:

$$\sigma_{\mathrm{y}}^2 = a_{21}^2\sigma_1^2 + a_{22}^2\sigma_2^2 + \cdots + a_{2n}^2\sigma_n^2 \tag{32}$$

$$\sigma_{\mathrm{z}}^2 = a_{31}^2\sigma_1^2 + a_{32}^2\sigma_2^2 + \cdots + a_{3n}^2\sigma_n^2 \tag{33}$$

b_{x}, b_{y}, and b_{z} denote the position errors. In accordance with (31), (32), and (33), we obtain the PED on each axis, i.e., $N(0, \sigma_{\mathrm{x}}^2)$, $N(0, \sigma_{\mathrm{y}}^2)$ and $N(0, \sigma_{\mathrm{z}}^2)$.

REFERENCES

[1] Q. Meng, J. Liu, Q. Zeng, S. Feng, and R. Xu, "Improved ARAIM fault modes determination scheme based on feedback structure with probability accumulation," *GPS Solutions*, vol. 23, no. 1, p. 11, Jan. 2019.
[2] L. Li, H. Wang, C. Jia, L. Zhao, and Y. Zhao, "Integrity and continuity allocation for the RAIM with multiple constellations," *GPS Solutions*, vol. 21, no. 4, pp. 1503–1513, Oct. 2017.
[3] J. Blanch, T. Walker, P. Enge, Y. Lee, B. Pervan, M. Rippl, A. Spletter, and V. Kropp, "Baseline advanced RAIM user algorithm and possible improvements," *IEEE Trans. Aerosp. Electron. Syst.*, vol. 51, no. 1, pp. 713–732, Jan. 2015.
[4] J. Blanch, T. Walter, and P. Enge, "Protection levels after fault exclusion for advanced RAIM," *Navigation*, vol. 64, no. 4, pp. 505–513, Dec. 2017.
[5] Y. Wu, X. Liu, W. Liu, J. Ren, Y. Lou, X. Dai, and X. Fang, "Long-term behavior and statistical characterization of BeiDou signal-in-space errors," *GPS Solutions*, vol. 21, no. 4, pp. 1907–1922, Oct. 2017.
[6] J. Blanch, T. Walter, and P. Enge, "Optimal positioning for advanced RAIM," *Navigation*, vol. 60, no. 4, pp. 279–289, Dec. 2013.
[7] B. W. Parkinson and P. Axelrad, "Autonomous GPS integrity monitoring using the pseudorange residual," *Navigation*, vol. 35, no. 2, pp. 255–274, Jun. 1988.
[8] D. Song, C. Shi, Z. Wang, C. Wang, and G. Jing, "Correlation-weighted least squares residual algorithm for RAIM," *Chin. J. Aeronaut.*, vol. 33, no. 5, pp. 1505–1516, May 2020.
[9] M. A. Sturza, "Navigation system integrity monitoring using redundant measurements," *Navigation*, vol. 35, no. 4, pp. 483–501, Dec. 1988.
[10] M. Joerger, S. Stevanovic, S. Langel, and B. Pervan, "Integrity risk minimisation in RAIM part 1: Optimal detector design," *J. Navigat.*, vol. 69, no. 3, pp. 449–467, May 2016.
[11] R. G. Brown, "A baseline GPS RAIM scheme and a note on the equivalence of three RAIM methods," *Navigation*, vol. 39, no. 3, pp. 301–316, Sep. 1992.
[12] A. T. S. C. Working Group C. *EU-U.S. Cooperation on Satellite Navigation Working Group C-ARAIM Technical Subgroup Milestone 2 Report Final Version*. Accessed: Feb. 23, 2017. [Online]. Available: https://www.gps.gov/policy/cooperation/europe/2015/working-group-c/ARAIM-milestone-2-report.pdf
[13] A. T. S. C. Working Group C. *EU-U.S. Cooperation on Satellite Navigation Working Group C-ARAIM Technical Subgroup Milestone 3 Report Final Version*. Accessed: Feb. 23, 2017. [Online]. Available: https://www.gps.gov/policy/cooperation/europe/2016/working-group-c/
[14] C. Milner and B. Pervan, "Bounding fault probabilities for advanced RAIM," *IEEE Trans. Aerosp. Electron. Syst.*, vol. 56, no. 4, pp. 2947–2958, Aug. 2020.
[15] P. Zhao, Y. Zhu, R. Xue, and L. Zheng, "Parity space projection line based fault detection method for advanced receiver autonomous integrity monitoring," *IEEE Access*, vol. 6, pp. 40836–40845, 2018.
[16] A. T. S. C. Working Group C. *EU-U.S. Cooperation on Satellite Navigation Working Group C, ARAIM Technical Subgroup Interim Report Issue 1.0*. Accessed: Feb. 20, 2017. [Online]. Available: https://www.gps.gov/policy/cooperation/europe/2013/working-group-c/
[17] H. Pesonen, "A framework for Bayesian receiver autonomous integrity monitoring in urban navigation," *Navigation*, vol. 58, no. 3, pp. 229–240, Sep. 2011.
[18] Q. Zhang and Q. Gui, "A new Bayesian RAIM for multiple faults detection and exclusion in GNSS," *J. Navigat.*, vol. 68, no. 3, pp. 465–479, May 2015.
[19] Y. Sun, "RAIM-NET: A deep neural network for receiver autonomous integrity monitoring," *Remote Sens.*, vol. 12, no. 9, p. 15, May 2020.
[20] Y. Yang and J. Xu, "GNSS receiver autonomous integrity monitoring (RAIM) algorithm based on robust estimation," *Geodesy Geodynamics*, vol. 7, no. 2, pp. 117–123, Mar. 2016.
[21] S. Hewitson and J. Wang, "GNSS receiver autonomous integrity monitoring (RAIM) performance analysis," *GPS Solutions*, vol. 10, no. 3, pp. 155–170, Jul. 2006.
[22] X. Zheng, Y. Liu, G. Fan, J. Zhao, and C. Xu, "Analyses of the sensitivity of multi-constellation advanced receiver autonomous integrity monitoring vertical protection level availability to error parameters and a failure model over China," *Adv. Mech. Eng.*, vol. 10, no. 6, p. 11, Jun. 2018.
[23] X. Sun, L. Xu, Y. Ji, W. Fu, S. Yan, and Q. Chen, "An extremum approximation ARAIM algorithm based on GPS and BDS," *IEEE Access*, vol. 8, pp. 30027–30036, 2020.

[24] J. Zhao, D. Song, C. Xu, and X. Zheng, "A modified LSR algorithm based on the critical value of characteristic slopes for RAIM," *IEEE Access*, vol. 7, pp. 70102–70116, 2019.
[25] G. Panel. *Phase II of the GNSS Evolutionary Architecture Study*. Accessed: May 5, 2016. [Online]. Available: https://xueshu.baidu.com/
[26] C. Lu, Y. Wang, M. Ragulskis, and Y. Cheng, "Fault diagnosis for rotating machinery: A method based on image processing," *PLoS ONE*, vol. 11, no. 10, Oct. 2016, Art. no. e0164111.
[27] F. G. Panel. *GNSS Evolutionary Architecture Study: Phase I-Panel Report*. Accessed: May 20, 2016. [Online]. Available: https://xueshu.baidu.com/
[28] A. El-Mowafy and C. Yang, "Limited sensitivity analysis of ARAIM availability for LPV-200 over Australia using real data," *Adv. Space Res.*, vol. 57, no. 2, pp. 659–670, Jan. 15 2016.
[29] Q. Gui, Y. Gong, G. Li, and B. Li, "Detection of multiple gross errors based on variance inflation model," *Sci. Surveying Mapping*, vol. 31, no. 4, pp. 28–29 and 3, 2006.
[30] G. Wübbeler, O. Bodnar, and C. Elster, "Bayesian hypothesis testing for key comparisons," *Metrologia*, vol. 53, no. 4, pp. 1131–1138, Aug. 2016.
[31] L. Wang, S. Luo, R. Tu, L. Fan, and Y. Zhang, "ARAIM with BDS in the Asia–Pacific region," *Adv. Space Res.*, vol. 62, no. 3, pp. 707–720, Aug. 2018.
[32] Q. Liu, H. Wang, X. Yi, Z. Yang, and X. Wang, "Weibull distribution features and application of sample standard deviation for normal fatigue matrix," *Mech. Sci. Technol. Aerosp. Eng.*, vol. 34, no. 7, pp. 1117–1122, 2015.
[33] P. Porwik, R. Doroz, and T. Orczyk, "Signatures verification based on PNN classifier optimised by PSO algorithm," *Pattern Recognit.*, vol. 60, pp. 998–1014, Dec. 2016.
[34] M. Behnam and H. Pourghassem, "Spectral correlation power-based seizure detection using statistical multi-level dimensionality reduction and PSO-PNN optimization algorithm," *IETE J. Res.*, vol. 63, no. 5, pp. 736–753, Sep. 2017.
[35] E. Wang, C. Jia, G. Tong, P. Qu, X. Lan, and T. Pang, "Fault detection and isolation in GPS receiver autonomous integrity monitoring based on chaos particle swarm optimization-particle filter algorithm," *Adv. Space Res.*, vol. 61, no. 5, pp. 1260–1272, Mar. 2018.
[36] M. Joerger, S. Langel, and B. Pervan, "Integrity risk minimisation in RAIM part 2: Optimal estimator design," *J. Navigat.*, vol. 69, no. 4, pp. 709–728, Jul. 2016.

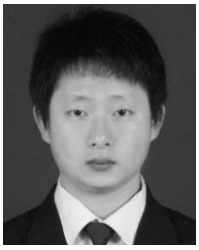

XUEEN ZHENG received the Ph.D. degree in aeronautical and astronautical science and technology from the Beijing Institute of Technology, Beijing, China, in 2019. He is currently holds a postdoctoral position with the School of Mechatronical Engineering, Beijing Institute of Technology, under the guidance of Prof. Y. Xu. His research interests include GNSS integrity, ANN, and unmanned aerial vehicle systems.

CHENGDONG XU received the Ph.D. degree from Beihang University, Beijing, China. He is currently a Professor with the School of Aerospace Engineering, Beijing Institute of Technology, Beijing. His research interests include aircraft design, digital design and manufacturing, satellite navigation, and system simulation.

YUDONG WANG received the B.Eng. and M.Eng. degrees in aeronautical and astronautical science and technology from the Beijing Institute of Technology, Beijing, in 2016 and 2020, respectively. Since 2020, he has been working with the Beijing Aerospace Long March Aircraft Research Institute, as an Assistant Engineer. His research interests include receiver autonomous integrity monitoring, satellite navigation, and flight dynamics.

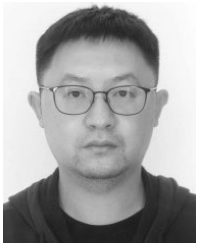

HAOMING ZOU received the Ph.D. degree from the Beijing Institute of Technology, Beijing, China, in 2017. He is currently a Researcher with the School of Materials Science and Engineering, Beijing Institute of Technology. His research interests include unmanned aerial vehicle materials and digital design.

XIJUAN LV received the Ph.D. degree from the Beijing Institute of Technology, Beijing, China, in 2018. She is currently holds a postdoctoral position with the Beijing Institute of Technology, under the guidance of Prof. Q. Shu. Her research interest includes unmanned aerial vehicle design and application.

SHUAI ZHAO received the B.E. degree from the Taiyuan University of Technology, Taiyuan, China, in 2016. He is currently pursuing the Ph.D. degree with the Beijing Institute of Technology, Beijing, China. His research interest includes the application in the field of ion detection and unmanned aerial vehicle application.

YANSONG SHI received the B.S. degree in materials engineering from the China University of Petroleum (East China), Shandong, China, in 2016, and the M.S. degree from the China University of Mining and Technology, Beijing, China, in 2019. He is currently pursuing the Ph.D. degree with the Beijing Institute of Technology, Beijing. His research interest includes basic research on analysis of unmanned aerial vehicle systems.

QINGHAI SHU received the Ph.D. degree from the University of Siegen, Germany, in 2012, under the supervision of Prof. Dr. Michael Schmittel. In 2013, he joined the Beijing Institute of Technology, as an Assistant Professor, where he focuses on unmanned aerial vehicle design and application.